Noda and Yamamoto
Earth, Planets and Space (2024) 76:155
https://doi.org/10.1186/s40623-024-02100-w

Earth, Planets and Space

FULL PAPER

Open Access

Homoclinic bifurcation of a rate-weakening patch in a viscoelastic medium and effect of strength contrast

Hiroyuki Noda[1*] and Makoto Yamamoto[2]

Abstract

The time-dependent viscoelastic deformation of host rocks is important when considering the dynamics of fault behavior, specifically in brittle–ductile transitional regions or shallow subduction zones, because it relaxes stress heterogeneity and affects loading to the fault. For a rate-and-state fault embedded in a Maxwell viscoelastic medium, a previous study discovered a transition from repeated earthquakes to the permanent stuck of a rate-weakening patch (EQ–ST transition) with decreased viscoelastic relaxation time t_c. This transition differs from the well-known seismic–aseismic transition explained by the Hopf bifurcation at the critical stiffness of an elastic system. To better understand the EQ–ST transition, quantifying the effect of heterogeneous frictional strength is important, because this effect is characteristic to the viscoelastic medium and is absent in the elastic limit. Previous experimental studies suggest a potential contrast in frictional strength Δf_* in such a way that a rate-weakening patch is stronger than a rate-strengthening region containing clay minerals. Here, we conducted two-dimensional, fully dynamic earthquake sequence simulations for a fault in a Maxwell viscoelastic medium; we investigated the EQ–ST transition in the two-dimensional parameter space of t_c and Δf_*. With $\Delta f_* = 0.3$, the EQ–ST transition occurred at about 1 order of magnitude larger t_c than in the case with $\Delta f_* = 0$. We constructed a coarse-grained model with only two degrees of freedom based on the spatial average. Consequently, the coarse-grained model behaves remarkably similar to the continuum model, and the EQ–ST transition is associated with a homoclinic bifurcation. The EQ–ST boundary in the parameter space can be quantitatively explained by considering elastic loading due to creep in the rate-strengthening region and unloading by viscoelastic relaxation of the stress heterogeneity comparable to Δf_*. A larger rate-weakening patch is anticipated to become aseismic earlier as t_c decreases, because the elastic loading rate is inversely correlated with the patch size. This may be qualitatively consistent with the change in the size distribution of events around the brittle–ductile transition in observations and laboratory experiments; however, further investigations on, for example, the interactions of events and changes in frictional parameters with depth are required for quantitative discussion.

Keywords Viscoelasticity, Numerical simulation, Earthquake sequence, SBIEM, Homoclinic bifurcation, Frictional strength

*Correspondence:
Hiroyuki Noda
noda.hiroyuki.7z@kyoto-u.ac.jp
Full list of author information is available at the end of the article

Graphical abstract

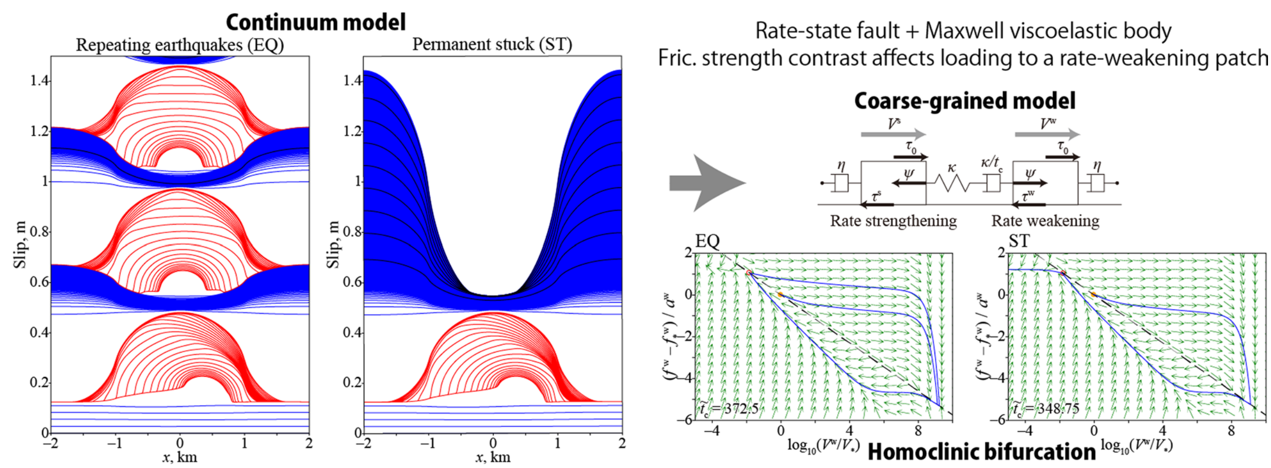

1 Introduction

Investigating the effects of inelastic deformation of the host rocks of an active fault is of great importance for understanding the dynamics of fault motion. Inelastic deformation plays an important role at different timescales in various ways. In the coseismic timescale, the stress concentration around a dynamically propagating rupture front may cause failure of the host rock (off-fault plasticity), which contributes to the fracture energy and prevents the rupture speed from approaching the terminal value (e.g., Andrews 2005). The localization of plastic deformation leads to the geometrical complexity of a fault system (Ando and Yamashita 2007; Templeton and Rice 2008; Okubo et al. 2019). Over a longer timescale, time-dependent viscous deformation causes relaxation of the deviatoric stress (viscoelastic relaxation, VR), which can be observed as post-seismic deformation (e.g., Savage and Prescott 1978; Thatcher and Rundle 1984; Moore et al. 2017; Johnson and Tebo 2018). Interseismically, it affects the loading process of the active fault (Iio et al. 2002) and the seismic cycle behavior (Wang et al. 2012). This study focused on the long-timescale effect modeled by the viscoelasticity of the host rock.

The slow earthquakes have timescales (e.g., duration and recurrence interval) between the above-mentioned endmember timescales and have been observed worldwide in many seismic–aseismic transitional regions (e.g., Obara and Kato 2016 for subduction, Shelly 2009 for a strike–slip fault). They are often explained by the frictional properties of the fault, such as modestly smaller elastic stiffness or larger patch size than the critical value (e.g., Kato 2003; Liu and Rice 2007), supercritical Hopf bifurcation in simplified spring–slider models (e.g., Gu et al. 1984), and changes in the signature of the rate dependency of shear resistance due to various mechanisms (e.g., Segall and Rice 1995; Shibazaki and Shimamoto 2007; Segall et al. 2010; Noda et al. 2017). Another potential factor dictating the mode of fault motion is viscous deformation. This may be important in the brittle–ductile transitional region where diffused deformation coexists with fault slip and in very shallow subduction zones where incohesive sediments undergo diagenesis. Previous simulation studies have revealed that viscoelastic deformation in the vicinity of a fault is important in determining the behavior of the fault among repeating earthquakes (EQ), repeating aseismic transients (AT), steady-state slip (SS), and permanent stuck (ST) (Allison and Dunham 2018; Goswami and Barbot; 2018; Miyake and Noda 2019). Miyake and Noda (2019) developed a methodology for a fully dynamic earthquake sequence simulation (ESS) accounting for interseismic VR in a Maxwell linear viscoelastic medium for anti-plane problems and investigated the transition among these behaviors. In addition to an increase in the characteristic length in the friction law, VR stabilizes the fault behavior from the EQ to the SS via AT only if the nucleation size in the elastic limit is slightly smaller than the patch size. A more brittle patch transitioned from EQ to ST, in which the slip rate of the rate-weakening patch asymptotically decreases to zero. The transition between AT and SS owing to VR was explained by the Hopf bifurcation of a simplified system (Miyake and Noda 2019); however, the transition between EQ and ST remains to be explained.

In the ESS conducted by Miyake and Noda (2019), using a rate- and state-dependent friction law, they assumed a uniform steady-state frictional strength f_* at a reference slip rate $V_* = 10^{-9}\mathrm{m/s}$ for simplicity. This assumption is not relevant for ESS with a linear elastic medium. For an elastic medium, a static solution always exists for an arbitrary traction distribution on a fault. If normal stress times the frictional strength σf_* is heterogeneous, the result of ESS for a linearly elastic medium can be constructed by superposing the corresponding static solution to the result of uniform σf_*. This superposition does not change the spatiotemporal distribution of the slip rate V and thus the fault behavior. However, heterogeneous traction on a planar fault relaxes in a viscoelastic medium. Subsequently, a static, time-invariant solution of heterogeneous traction does not exist, and we cannot obtain the result of ESS for heterogeneous σf_* by the simple superposition. Hence, the distribution of σf_* affects the fault behavior.

Clay minerals are known to have a much smaller friction coefficient than Byerlee's law (e.g., Byerlee 1978), and often show rate-strengthening properties (e.g., Saffer and Marone 2003) although the frictional properties depend on experimental conditions such as the slip rate, amount of slip, and internal structure (e.g., Beeler et al. 1996; Collettini et al. 2009; den Hartog et al. 2012; Sawai et al. 2016). Ikari et al. (2011) conducted friction experiments for various minerals, and concluded that the friction coefficient ranges from 0.5 to 0.7 for rate-weakening minerals and from 0.2 to 0.7 for rate-strengthening minerals. This argument might be too simplistic given the complex dependency of the frictional properties of the fault gouge under a wide range of deformation conditions; however, a contrast likely exists in the frictional strength between the rate-weakening and rate-strengthening regions. The effect of strength contrast on fault behavior remains unexplored in the context of an ESS for a viscoelastic medium. Note that the quantification and explanation of the effect of strength contrast are key to understanding the effect of VR, because it is characteristic of the viscoelastic system and absent in the elastic limit.

The present study was designed to address these two questions. The first is what the EQ–ST transition is. A continuum model has many degrees of freedom, and finding a rigorous explanation is not always easy. Therefore, we conducted additional simulations of a simplified coarse-grained model and compared the results. The continuum and simplified models were comparable in terms of averaged behavior inside a rate-weakening patch. In addition, the condition for the EQ–ST transition were qualitatively similar. Hence, we argue that the simplified model, which can be understood rigorously from the nonlinear dynamics perspective, explains the continuum model. The second question is how the strength contrast affects the fault behavior. This was investigated by conducting parameter studies regarding the strength contrast and relaxation time and deriving a formula predicting the EQ–ST boundary in the parameter space. This formula illuminates the physical role of VR in the EQ–ST transition.

2 Continuum model

2.1 Formulation

2.1.1 SBIEM for a Maxwell–viscoelastic medium

For an elastic medium, the shear traction on the fault τ can be expressed as

$$\tau(x,t) = \tau_0 + \phi^{\mathrm{EL}}[V](x,t) - \eta V(x,t), \tag{1}$$

where x represents the position along the fault, t is time, τ_0 is the shear traction that would be realized if there were no slip on the fault, η is given by $\mu/2c_\mathrm{s}$, μ is the shear modulus, c_s is the shear-wave speed, and V is the slip rate. In the present study, we assumed uniform τ_0, $\mu = 30\mathrm{GPa}$, and $c_\mathrm{s} = 3\mathrm{km/s}$. The last term represents the impedance effect, referred to as the radiation-damping effect (Rice 1993). $\phi^{\mathrm{EL}}[V]$ is a functional of previous slip rate expressed by spatio-temporal convolution. ϕ^{EL} can be split to static and dynamic terms:

$$\phi^{\mathrm{EL}} = \phi^{\mathrm{EL}}_{\mathrm{st}} + \phi^{\mathrm{EL}}_{\mathrm{dy}}. \tag{2}$$

$\phi^{\mathrm{EL}}_{\mathrm{st}}$ is spatial convolution of the current slip and the static Green's function:

$$\phi^{\mathrm{EL}}_{\mathrm{st}} = K_{\mathrm{st}} * \delta = \mathcal{F}^{-1}\left[-\frac{\mu|k|}{2}D\right], \tag{3}$$

where δ is the slip, K_{st} is the elastostatic Green's function, $\mathcal{F}$ is Fourier transformation with respect to x, k is the angular wavenumber, and D is the Fourier transform of δ. $\phi^{\mathrm{EL}}_{\mathrm{dy}}$ is, by definition, the difference between the static and dynamic solutions minus the radiation-damping effect and expressed as spatio-temporal convolution of previous V and a dynamic kernel (e.g., Rice and Ben-Zion 1996). Because contribution of old V to $\phi^{\mathrm{EL}}_{\mathrm{dy}}$ becomes negligible as the relative time increases, the temporal convolution for $\phi^{\mathrm{EL}}_{\mathrm{dy}}$ can be truncated and thus ESS is possible for a finite memory requirement. Lapusta et al. (2000) used a time window of 1–4 times the duration for a shear wave to travel the system length. We adopted a normalized time window of 3 after confirming some simulation results by comparing the cases with a halved time window. In previous studies (e.g., Rice and Ben-Zion 1996; Lapusta et al. 2000) δ, V, and ϕ were expressed in terms of Fourier basis, a Fast Fourier Transform technique was used for efficient numerical simulation.

Miyake and Noda (2019) modified the elastic ESS to implement interseismic VR in a Maxwell viscoelastic medium for anti-plane problems. Because a viscoelastic material reacts to instantaneous loading in the same manner as an elastic material, the radiation-damping effect must remain unchanged. Subsequently, the traction on the fault is written as

$$\tau = \tau_0 + \phi[V] - \eta V, \tag{4}$$

where ϕ is traction change due to previous fault motion. τ_0 is the shear stress that would be realized if the fault were glued up and VR were neglected. Similar to the elastic case ϕ was split into quasistatic effect ϕ_{st} and the difference from it ϕ_{dy}:

$$\phi = \phi_{\mathrm{st}} + \phi_{\mathrm{dy}}. \tag{5}$$

Because the coseismic timescale was too short that the viscoelastic effect was negligible, the dynamic part was assumed to be identical to that in the elastic case:

$$\phi_{\mathrm{dy}} = \phi_{\mathrm{dy}}^{\mathrm{EL}}. \tag{6}$$

The quasistatic part can be expressed by spatio-temporal convolution; however, Miyake and Noda (2019) went around the temporal convolution by using a memory variable, effective slip δ_{eff}:

$$\phi_{\mathrm{st}} = K_{\mathrm{st}} * \delta_{\mathrm{eff}} = \mathcal{F}^{-1}\left[-\frac{\mu|k|}{2}D_{\mathrm{eff}}\right]. \tag{7}$$

$$\dot{D}_{\mathrm{eff}} = \dot{D} - \frac{D_{\mathrm{eff}}}{t_{\mathrm{c}}}. \tag{8}$$

where the dots on top of variables represent time derivative, D_{eff} was Fourier transform of δ_{eff}, and t_{c} was the relaxation time of the Maxwell viscoelastic material. Equation (8) can be easily integrated at each time step. This study uses almost the same numerical method as Miyake and Noda (2019). The only difference is that Eq. (8) is integrated using an exponential time-differencing method based on a constant V or $\dot{D}$, similar to the state variable in the friction law (e.g., Noda and Lapusta 2010).

2.1.2 Friction law

Similar to Miyake and Noda (2019), we adopt an aging law (Dieterich 1979; Ruina 1983):

$$\tau = \sigma\left(f_* + a\ln\left(\frac{V}{V_*}\right) + b\ln(\theta)\right), \dot{\theta} = \frac{V}{L}\left(\frac{V_*}{V} - \theta\right), \tag{9}$$

where σ is the normal stress assumed to be 100 MPa, f_* is friction coefficient at a reference $V = V_* = 10^{-9}\mathrm{m/s}$, a and b are nondimensional parameters representing the direct and evolutionary effects, respectively, θ is the state variable and L is the characteristic slip of the state evolution. The steady-state friction coefficient changes by $a - b$ for an e-fold increase in V. Therefore, a point on the fault is called a rate strengthening or rate weakening if $a - b > 0$ and $a - b < 0$, respectively. We set up a rate-weakening patch embedded in the rate-strengthening region. For the rate-weakening patch, we assumed frictional parameters $a = a^{\mathrm{w}} = 0.016$, $b = b^{\mathrm{w}} = 0.02$ comparable to granite under seismogenic conditions (Blanpied et al. 1998), which obeys Byerlee's law. For the rate-strengthening region, we selected $a = a^{\mathrm{s}} = 0.005$, $b = b^{\mathrm{s}} = 0$, motivated by the extremely small evolutionary effect of the clay material (e.g., Ikari et al. 2009). Note that small amounts of non-clay (e.g., quartz) clasts yield a significant b comparable to a (e.g., Saffer and Marone (2003)). Still, the simplification of $b^{\mathrm{s}} = 0$ decreased the degree of freedom of the system and was very useful in interpreting nonlinear dynamics. The reference friction was set $f_* = f_*^{\mathrm{w}} = 0.6$ inside and $f_* = f_*^{\mathrm{s}} = 0.6 - \Delta f_*$ outside the rate-weakening patch. We refer $\Delta f_* (> 0)$ as the frictional strength contrast hereafter. a, b, and f_* were given by using a smoothed boxcar function (e.g., Noda and Lapusta 2010):

$$a = a^{\mathrm{s}} + \left(a^{\mathrm{w}} - a^{\mathrm{s}}\right)B(x, 0.9R, 0.2R), \tag{10}$$

$$b = b^{\mathrm{s}} + \left(b^{\mathrm{w}} - b^{\mathrm{s}}\right)B(x, 0.9R, 0.2R), \tag{11}$$

$$f_* = f_*^{\mathrm{s}} + \Delta f_* B(x, 0.9R, 0.2R), \tag{12}$$

$$B(x, W, w) = \begin{cases} 1 & |x| < W \\ \frac{1}{2} - \frac{1}{2}\tanh\left(\frac{w}{|x| - W - w} + \frac{w}{|x| - W}\right) & W \le |x| \le W + w \\ 0 & W + w < |x| \end{cases}. \tag{13}$$

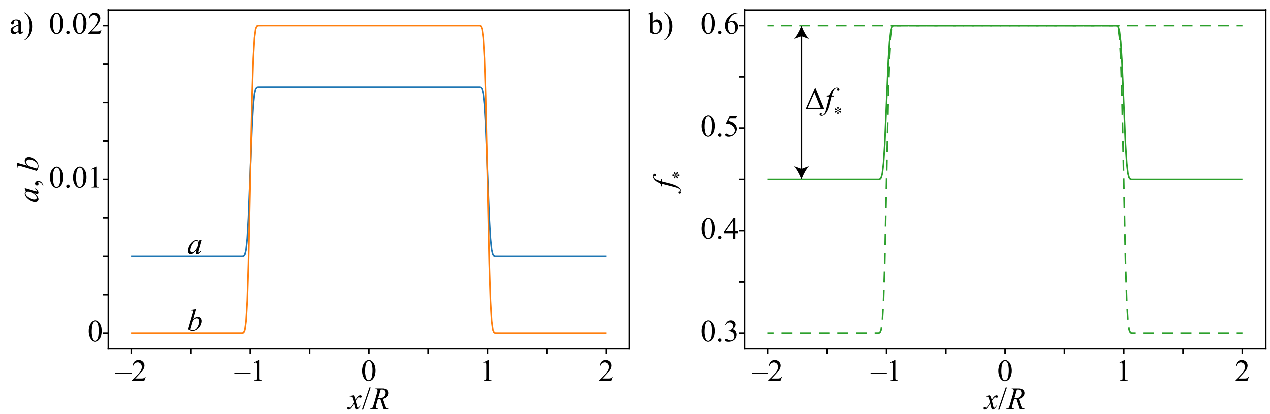

Fig. 1 Distribution of frictional properties. **a** Rate-dependency parameters, **b** friction coefficient at a reference $V_* = 10^{-9}$m/s. Δf_* is the frictional strength contrast

where R is approximately half the length of the rate-weakening patch (Fig. 1) and periodic boundaries were assumed every $4R$. L was set as uniform, and its value was selected by specifying the nucleation size (Rubin and Ampuero 2005):

$$R_\mathrm{c} = \frac{1}{\pi}\frac{b^\mathrm{w}}{(b^\mathrm{w} - a^\mathrm{w})^2}\frac{\mu L}{\sigma} = 0.4R. \tag{14}$$

The corresponding length scale of the process zone (Lapusta and Liu 2009) is as follows:

$$\Lambda_0 = \frac{9\pi}{32}\frac{\mu L}{b^\mathrm{w}\sigma} \approx 0.0444R. \tag{15}$$

We used 400 spatial grid points, so that

$$\Delta x = 0.01R \approx 4.44\Lambda_0, \tag{16}$$

This indicates the good spatial resolution of the present simulations (Day et al 2005).

The geophysically relevant stress scales (e.g., stress drop and rock stiffness) and speed (e.g., wave speeds and plate convergence rate) are relatively well constrained. In contrast, the scale of length, the remaining independent dimension, may vary by orders of magnitude, as indicated by the Gutenberg–Richter law in the size distribution of earthquakes. When visualizing the slip distribution on the fault, we chose a specific scale of $2R = 1$km for a presentational purpose.

2.2 Methodology

2.2.1 Boundary and initial conditions

In the present study, we conducted parameter studies in a parameter space $(t_c, \Delta f_*)$. We adopted a boundary condition similar to that used by Miyake and Noda (2019). As mentioned in the previous section, periodic boundaries were assumed every $4R$. A positive rate dependency on average prevents system-spanning ruptures (e.g., Dublanchet et al. 2013). The fault motion was driven by applying constant far-field shear stress τ_0, the selection of which shall be explained below. The initial conditions of the simulations were specified by giving $\theta_\mathrm{ini}(x)$ and τ_0.

Miyake and Noda (2019) reported that the fault behavior (EQ, AT, SS, or ST) depends on the initial conditions (see Fig. 10, in their paper). For a systematic parameter study, we started the simulations from a point close to steady-state solutions, which we numerically calculated for all sets of $(t_\mathrm{c}, \Delta f_*)$. For a fixed value of t_c, we set a regular mesh of an interval $\Delta f_*^i - \Delta f_*^{i-1} = 0.0125$ with $\Delta f_*^0 = 0$. For the cases with $\Delta f_* = 0$, there is a trivial uniform steady-state solution:

$$V = V_\mathrm{ss}^0 = V_*, \theta = \theta_\mathrm{ss}^0 = 1, \tau = \tau_\mathrm{ss}^0 = \sigma f_*^\mathrm{w}, \tag{17}$$

regardless of t_c. It leads to the initial condition:

$$\theta_\mathrm{ini}^0(x) = \theta_\mathrm{ss}^0 = 1, \tau_0^0 = \tau_\mathrm{ss}^0 + \eta V_\mathrm{ss}^0 = \sigma f_*^\mathrm{w} + \eta V_* \tag{18}$$

including the inevitable numerical round-off errors. An increase in Δf_* led to overall weakening of the fault so that the driving force τ_0 was decreased accordingly to keep the simulations comparable:

$$\tau_0^i = \sigma f_*^\mathrm{w} - \frac{\sigma \Delta f_*^i}{2} + \eta V_*. \tag{19}$$

Given an approximate steady-state solution for $\Delta f_* = \Delta f_*^{i-1}$, that for $\Delta f_* = \Delta f_*^i$ was calculated with a stabilized ESS by increasing L by a factor of 10 from Eq. (14). Owing to the linearity of the medium, Eq. (4) can be rewritten as follows:

$$\begin{aligned} \tau &= \tau_0 + \phi[V_\mathrm{ref} + \Delta V] - \eta(V_\mathrm{ref} + \Delta V) \\ &= \tau_\mathrm{ref} + \phi[\Delta V] - \eta\Delta V, \end{aligned} \tag{20}$$

where the subscript "ref" indicates a reference solution

$$\tau_{\mathrm{ref}} = \tau_0 + \phi[V_{\mathrm{ref}}] - \eta V_{\mathrm{ref}}, \tag{21}$$

and ΔV is the difference in the slip rate from the reference. A simulation code was set up to calculate Eq. (20) rather than Eq. (4) to enable simulations under potentially complex loading conditions. To clarify, V_{ref} is a reference in a linear viscoelastic solution and is different from the reference in rate- and state-dependent friction, V_*. The reference solution does not need to satisfy the friction law. The reformulation of Eqs. (4)–(20) is just reselection of a reference from which the displacement is measured, being called "back-slip formulation" in some circumstances. In computing the steady-state solution for $\Delta f_* = \Delta f_*^i$ with the stabilized ESS, we adopted V_{ss}^{i-1} as V_{ref}

$$\tau_{\mathrm{ref}} = \tau_0^i + \phi\left[V_{\mathrm{ss}}^{i-1}\right] - \eta V_{\mathrm{ss}}^{i-1} = \tau_{\mathrm{ss}}^{i-1} - \sigma\frac{\Delta f_*^i - \Delta f_*^{i-1}}{2}, \tag{22}$$

and $\theta_{\mathrm{ss}}^{i-1}$ as the initial value of θ. If the steady-state solution is continuous with respect to Δf_*, the initial condition is close to the steady state and the stabilized ESS is expected to decay to it quickly.

In many cases, the variables decayed towards the steady state, at which $\dot{V} = 0$, $\dot{\theta} = 0$, $\dot{\phi} = 0$, and $\dot{\tau} = 0$. From Eqs. (4) and (9), we have two constraints:

$$\dot{\tau} = \dot{\phi} - \eta\dot{V}, \tag{23}$$

$$\dot{\tau} = a\sigma\frac{\dot{V}}{V} + b\sigma\frac{\dot{\theta}}{\theta}. \tag{24}$$

Therefore, we checked only $\dot{V}$ and $\dot{\theta}$ to terminate the stabilized ESS. Because $\eta \ll a\sigma/V$ in the interseismic processes and the steady-state solutions of our interest here, we halted the stabilized ESS when both $\left|\dot{V}/V\right|$ and $b/a\left|\dot{\theta}/\theta\right|$ becomes smaller than $10^{-6}\mathrm{s}^{-1}$. θ in the final snapshot was regarded as the steady-state values θ_{ss}^i and used to specify the initial condition:

$$\theta_{\mathrm{ini}}^i(x) = \theta_{\mathrm{ss}}^i(x). \tag{25}$$

For large values of Δf, the condition for steady state failed to be satisfied before $t = 10{,}000\mathrm{yr}$. At this point, we halted the simulation and gave up a parameter study, classifying the remaining cases as "No steady state obtained" (NoSS). Although the criterion for a steady state adopted here is artificial, the simulations in the present study appear reasonable.

2.2.2 *Procedure of parameter study*

For Δf_*, we covered a range from 0 to 0.3 corresponding to f_s from 0.6 to 0.3. For t_{c}, Miyake and Noda (2019) defined a non-dimensional relaxation time by comparing t_{c} with the time scale of elastic loading by a surrounding creeping rate-strengthening region:

$$\widetilde{t}_{\mathrm{c}} = \frac{t_{\mathrm{c}}\mu V_*}{2R\sigma a^{\mathrm{w}}}. \tag{26}$$

In this expression, the creep rate was assumed to be V_*, which may be reasonable for $\Delta f_* = 0$, because the steady-state solution with $V = V_*$ exists (Eq. 17). However, the creep rate may be significantly higher in the present study, because the rate-strengthening region is weaker. The redefinition of the non-dimensional relaxation time is one of the goals of this study; however, t_{c} for the parameter study is specified in Eq. (26). We conducted a parameter study for $40 \le \widetilde{t}_{\mathrm{c}} \le 610$ with 25 regularly spaced grid points. This range was determined to capture the EQ–ST boundary in the range of Δf_* studied.

Earthquake ruptures were defined by a threshold of the spatial maximum V of $0.1\mathrm{m/s}$. T_i denotes the interval between the ith and $(i-1)$ th earthquakes, and we stopped the simulation when $|T_i/T_{i-1} - 1| < 10^{-3}$, classifying the case as EQ and defining the recurrence interval $T_{\mathrm{r}} = T_i$. Otherwise, we stopped the simulation when the spatial minimum V became smaller than $10^{-5}V_* = 10^{-14}\mathrm{m/s}$, classifying the case as ST.

2.3 Simulation results

Figure 2 shows the result of the parameter study. The recurrence interval T_{r} normalized by that in the elastic

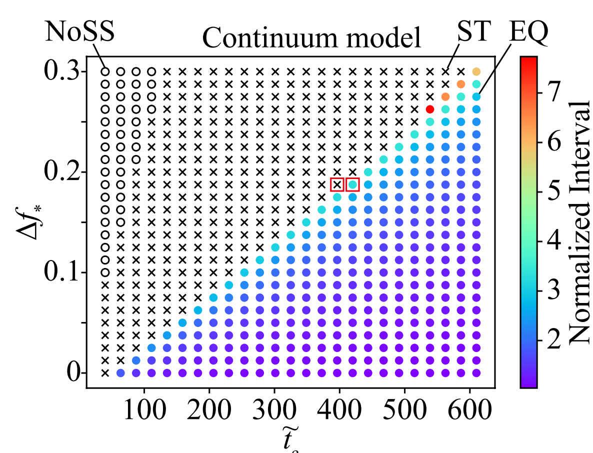

Fig. 2 Result of parameter study for the continuum model. Colors indicate the recurrence interval T_{r} normalized by in the elastic limit. Black crosses and open circles represent permanent stuck and no steady-state solution, respectively. Cases with red squares are plotted in Fig. 3

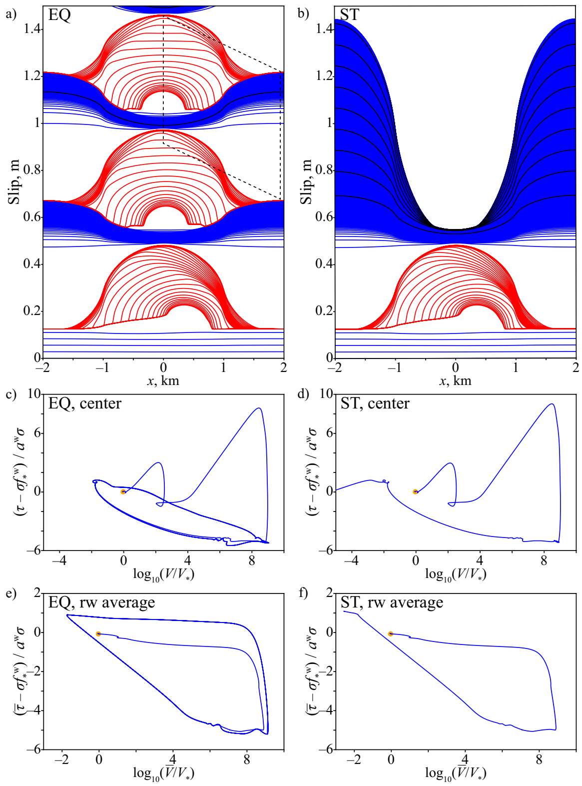

Fig. 3 Example simulations of EQ (left) and ST (right) cases indicated by red squares in Fig. 2 ($\Delta f_* = 0.1875$). **a, b** Cumulative slip distribution. Red, blue, and black lines are plotted every 0.03 (coseismically), 3×10^7, and 3×10^9 s, respectively. A dashed parallelogram in (**a**) shows difference in long-term slip rate. **c, d** Trajectories of shear stress and slip rate at the center of the rate-weakening patch. **e, f** Trajectories of averaged shear stress and slip rate in the rate-weakening patch

limit is colored for EQ; ST and NoSS are indicated by black crosses and open circles, respectively. The boundary between ST and NoSS is not defined by the simulation behavior, but by the failure of finding the unstable steady-state solution used as the initial condition (Sect. 2.1.1.). Similar to efficient VR, the strength contrast increases T_r and promotes the permanent stuck of the rate-weakening patch. The case with $\Delta f_* = 0.3$ shows the EQ–ST transition at about one order of magnitude larger $\widetilde{t}_c$ than the case without the strength contrast. One of the goals of the present study was to understand the apparent linear boundary between EQ and ST.

A pair of EQ and ST cases just across the boundary with $\Delta f_* = 0.1875$ indicated by red squares in Fig. 2 are shown in Fig. 3. In the EQ case (Fig. 3a), the rate-weakening patch repeatedly generated earthquake ruptures. The dashed parallelogram shows that the long-term slip rate was lower in the rate-weakening patch. In the ST case (Fig. 3b), the patch eventually stopped slipping. Figure 3c, d shows the trajectories of the shear stress versus the slip rate at the center of the patch. In both cases, as soon as the simulation began, a minor acceleration event occurred before the second acceleration towards the coseismic slip rate. The almost linear trends in acceleration shown in Fig. 3c, d indicate rapid stressing in front of the rupture and creep fronts. Indeed, the nucleation of the first earthquake rupture occurred slightly off-center. In the EQ case, after the first rupture, V decreased to a minimum value of approximately $10^{-2}V_*$ during the interseismic period, followed by an acceleration towards the second rupture. The trajectory quickly settled to the limit cycle and the simulation was halted after the fourth rupture. In the ST case, the behavior is quite similar before V reaches about $10^{-2}V_*$ after the earthquake rupture. From this point, V further decreased with decreasing τ and reached $10^{-5}V_*$ where the simulation was halted. The trajectories in Fig. 3c, d intersect with itself; hence, explaining such detailed behavior requires more than three degrees of freedom.

We took spatial average of the shear stress τ and the slip rate V over the rate-weakening patch $-R < x < R$ ($\overline{\tau}$ and $\overline{V}$). Subsequently, the trajectories were significantly simplified (Fig. 3e, f). The sharp increases and decreases in τ before the 1st rupture disappeared, which reflected small-scale behavior interior of the patch. In addition, the self-intersections of the trajectories were minimized. We adopted these trajectories as the coarse-grained behavior of the system. We attempted to reproduce them using a simpler system with two degrees of freedom to draw a physical understanding of the combined effect of VR and strength contrast.

3 Coarse-grained model

3.1 Formulation

The continuum model has infinite degrees of freedom; thus, a rigorous mathematical discussion is difficult. A simplified system was used for comparison to interpret the results of the continuum model.

Averaging of Eq. (4) inside and outside the rate-weakening patch yields

$$\tau^{\mathrm{w}} = \tau_0 + \phi^{\mathrm{w}} - \eta V^{\mathrm{w}}, \tag{27}$$

$$\tau^{\mathrm{s}} = \tau_0 + \phi^{\mathrm{s}} - \eta V^{\mathrm{s}}. \tag{28}$$

where the superscripts w and s represent the average values in the rate-weakening and rate-strength regions, respectively. Because the integral of ϕ over the infinite fault plane is zero, we simplify the notation using

$$\psi = \phi^{\mathrm{w}} = -\phi^{\mathrm{s}}. \tag{29}$$

In the continuum model described in the last section, ψ includes contributions not only from ϕ_{st}, but also from ϕ_{dy}. In the simplified model, we ignored the latter contribution. It may be significant during dynamic events; however, they are most likely negligible during the interseismic period, in which deceleration towards the stuck state was observed.

We assumed that the fault motion can be divided into two parts:

$$V(x) = V^{w}\Omega_{w}(x) + V^{s}\Omega_{s}(x), \tag{30}$$

where Ω_w and Ω_s are characteristic shape functions of slip rate distribution in the rate-weakening and rate-strengthening regions, respectively, satisfying

$$\Omega_{w}(x) + \Omega_{s}(x) = 1. \tag{31}$$

The effective slip in the space domain evolves as (Eq. 8)

$$\dot{\delta}_{eff} = V - \frac{\delta_{eff}}{t_c}. \tag{32}$$

Because this is a linear equation, the same shape functions can be naturally used for δ_{eff}

$$\delta_{eff}(x) = \delta_{eff}^{w}\Omega_{w}(x) + \delta_{eff}^{s}\Omega_{s}(x) \tag{33}$$

hence, the averaged effective slips evolve as

$$\dot{\delta}_{eff}^{w} = V^{w} - \frac{\delta_{eff}^{w}}{t_c}, \dot{\delta}_{eff}^{s} = V^{s} - \frac{\delta_{eff}^{s}}{t_c}. \tag{34}$$

Equation (7) can be written as

$$\begin{aligned}\phi_{st}(x) &= \int_{-2R}^{2R} \widetilde{K}_{st}(x-x')\delta_{eff}(x')dx' \\ &= \delta_{eff}^{w}\int_{-2R}^{2R} \widetilde{K}_{st}(x-x')\Omega_{w}(x)dx' \\ &\quad + \delta_{eff}^{s}\int_{-2R}^{2R} \widetilde{K}_{st}(x-x')\Omega_{s}(x)dx'.\end{aligned} \tag{35}$$

Note that $\widetilde{K}_{st}$ is different from K_{st} in Eq. (7) in that periodic replication of the source with an interval $4R$ was assumed. It satisfies

$$\widetilde{K}_{st}(x) = \widetilde{K}_{st}(x+4R), \quad \int_{-2R}^{2R} \widetilde{K}_{st}(x)dx = 0, \tag{36}$$

Averaging Eq. (35) inside and outside the rate-weakening patch, we obtain:

$$\phi^{w} = \psi = \delta_{eff}^{w}K_{w}^{w} + \delta_{eff}^{s}K_{s}^{w}, \phi^{s} = -\psi = \delta_{eff}^{w}K_{w}^{s} + \delta_{eff}^{s}K_{s}^{s} \tag{37}$$

where

$$\begin{aligned}K_{w}^{w} &= \frac{1}{2R}\int_{-R}^{R} dx \int_{-2R}^{2R} K_{st}(x-x')\Omega_{w}(x)dx' \\ K_{s}^{w} &= \frac{1}{2R}\int_{-R}^{R} dx \int_{-2R}^{2R} K_{st}(x-x')\Omega_{s}(x)dx' \\ K_{w}^{s} &= \frac{1}{2R}\left[\int_{-2R}^{2R} dx - \int_{-R}^{R} dx\right]\int_{-2R}^{2R} K_{st}(x-x')\Omega_{w}(x)dx' \\ K_{s}^{s} &= \frac{1}{2R}\left[\int_{-2R}^{2R} dx - \int_{-R}^{R} dx\right]\int_{-2R}^{2R} K_{st}(x-x')\Omega_{s}(x)dx'\end{aligned} \tag{38}$$

First

$$\begin{aligned}K_{w}^{w} + K_{w}^{s} &= \frac{1}{2R}\int_{-2R}^{2R} dx \int_{-2R}^{2R} K_{st}(x-x')\Omega_{w}(x)dx' = 0 \\ K_{s}^{w} + K_{s}^{s} &= \frac{1}{2R}\int_{-R}^{R} dx \int_{-2R}^{2R} K_{st}(x-x')\Omega_{s}(x)dx' = 0\end{aligned} \tag{39}$$

because of Eq. (36). Second, Eqs. (31) and (36) yield

$$\begin{aligned}K_{w}^{w} + K_{s}^{w} &= \frac{1}{2R}\int_{-R}^{R} dx \int_{-2R}^{2R} K_{st}(x-x')dx' = 0 \\ K_{w}^{s} + K_{s}^{s} &= \frac{1}{2R}\left[\int_{-2R}^{2R} dx - \int_{-R}^{R} dx\right]\int_{-2R}^{2R} K_{st}(x-x')dx' = 0\end{aligned} \tag{40}$$

Therefore, only one stiffness parameter exists

$$\kappa = K_{s}^{w} = -K_{w}^{w} = K_{w}^{s} = -K_{s}^{s}. \tag{41}$$

ψ can then be written as

$$\psi = \kappa\left(\delta_{eff}^{s} - \delta_{eff}^{w}\right) \tag{42}$$

and its evolution, as

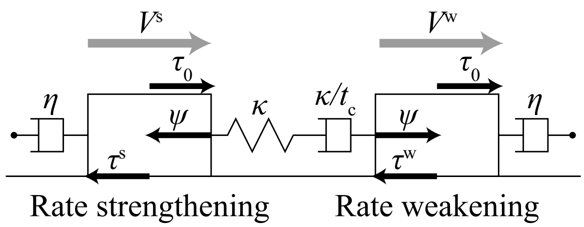

Fig. 4 Schematic diagram of the spring–slider–dashpot system expressed by Eqs. (43)–(45)

$$\dot{\psi} = \kappa\left(V^s - V^w\right) - \frac{\psi}{t_c}. \tag{43}$$

Equations (27), (28), (29) yield

$$\tau^w = \tau_0 + \psi - \eta V^w, \tag{44}$$

$$\tau^s = \tau_0 - \psi - \eta V^s. \tag{45}$$

These equations and Eq. (43) can be regarded as a spring–slider–dashpot system (Fig. 4), which is identical to the system studied by Miyake and Noda (2019) in terms of the stability of steady-state solutions. Stiffness κ should be expressed as

$$\kappa = \gamma\frac{\mu}{2R}. \tag{46}$$

where γ is a geometrical factor around 1 and depends on Ω_w and Ω_s. These shape functions are approximations of the actual distribution of V in the continuum model under certain circumstances, such as during coseismic or inter-seismic periods, and are difficult to determine. Miyake and Noda (2019) quantitatively explain the stability change of the steady-state solution by $\gamma = 0.97$, which was adopted in the present study.

For the friction law, we assumed that the aging law holds for the averaged traction and slip rates:

$$\tau^w = \sigma\left(f_*^w + a^w\ln\frac{V^w}{V_*} + b^w\ln\theta^w\right), \dot{\theta}^w = \frac{V^w}{L}\left(\frac{V_*}{V^w} - \theta^w\right), \tag{47}$$

$$\tau^s = \sigma\left(f_*^s + a^s\ln\frac{V^s}{V_*}\right) = \sigma\left(f_*^w + \Delta f_* + a^s\ln\frac{V^s}{V_0}\right). \tag{48}$$

If we give ψ and θ^w, then we can solve Eqs. (44) and (47) for τ^w and V^w, and Eqs. (45) and (48) for τ^s and V^s. Therefore, the dynamical system has two degrees of freedom and can be completely visualized in a two-dimensional phase space (plane).

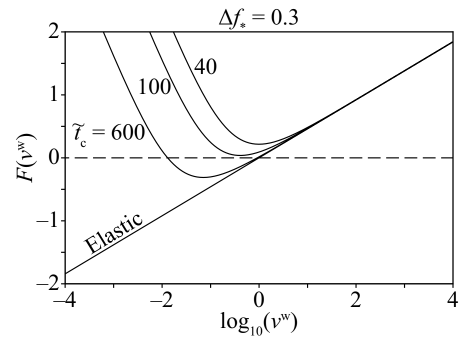

Fig. 5 Examples of $F(\nu^W)$ [Eq. (54)]. $F(\nu^W) = 0$ at the steady-state solutions

3.2 Methodology

The system of Eqs. (43–45), (Eq. 47), and (Eq. 48) are solved numerically. We chose $\Theta = \ln(\theta^w)$ and ψ as the independent set of variables for time integration. ψ and Θ evolves as Eq. (43) and

$$\frac{d\Theta}{dt} = \frac{V_*}{L}\exp(-\Theta) + \frac{V^w}{L}, \tag{49}$$

respectively. V^w and V^s can be expressed in terms of these variables by solving Eqs. (44), (45), (47), and (48) using the Lambert W function. The time integration was executed using scipy.integrate.solve_ivp with 'Radau' method, a fifth-order implicit Runge–Kutta method with a third-order numerical error control. We used relative tolerance of 10^{-9}. For a parameter study comparable to the continuum model, the initial condition was selected to be close to a steady-state solution, which must be estimated, as explained below.

At steady state, Eqs. (43), (47), (48) yield

$$\psi = \kappa t_c V_*\left(\nu^s - \nu^w\right) \tag{50}$$

$$f^w = f_*^w + \left(a^w - b^w\right)\ln\nu^w, \tag{51}$$

$$f^s = f_*^w - \Delta f_* + a^s\ln\nu^s, \tag{52}$$

where $\nu = V/V_*$, $f = \tau/\sigma$, and superscripts w and s indicate spatial average inside and outside the rate-weakening patch, respectively. Equations (19), (26), (44), (46), (50) and (51) yield

$$\nu^s\left(\nu^w\right) = \nu^w + \frac{a^w - b^w}{\gamma\widetilde{t}_c a^w}\ln\nu^w + \frac{\eta V_*}{\gamma\widetilde{t}_c a^w\sigma}\left(\nu^w - 1\right) + \frac{\Delta f_*}{2\gamma\widetilde{t}_c a^w}. \tag{53}$$

Equations (19), (26), (45), (47), (50), and (52) yield

$$F\left(\nu^w\right) = \ln\nu^s + \frac{\gamma\widetilde{t}_c a^w}{a^s}\left(\nu^s - \nu^w\right) + \frac{\eta V_*}{a^s\sigma}\left(\nu^s - 1\right) - \frac{\Delta f_*}{2a^s} = 0, \tag{54}$$

where v^{s} in Eq. (54) is a function of v^{w} given by Eq. (53). A steady-state solution can be obtained by finding zeros of $F(v^{\mathrm{w}})$. In the elastic limit $\widetilde{t}_{\mathrm{c}} \to \infty$, F is given by

$$F\left(v^{\mathrm{w}}\right) \to \frac{a^{\mathrm{s}} + a^{\mathrm{w}} - b^{\mathrm{w}}}{a^{\mathrm{s}}} \ln v^{\mathrm{w}} + 2\frac{\eta V_*}{\sigma a^{\mathrm{s}}}\left(v^{\mathrm{w}} - 1\right) = 0, \tag{55}$$

which has only one solution $v^{\mathrm{w}} = 1$, because $a^{\mathrm{s}} + a^{\mathrm{w}} - b^{\mathrm{w}} > 0$.

Figure 5 shows $F(v^{\mathrm{w}})$ for various $\widetilde{t}_{\mathrm{c}}$ with $\Delta f_* = 0.3$ as an example. VR increases $F(v^{\mathrm{w}})$ at small v^{w}. If $\widetilde{t}_{\mathrm{c}}$ is large yet finite, two solutions can be made. The larger one is close to the elastic solution $v^{\mathrm{w}} = 1$, and the other is much smaller. As $\widetilde{t}_{\mathrm{c}}$ decreases, these two solutions approach each other, collide, and disappear at critical $\widetilde{t}_{\mathrm{c}}$. This was a tangent bifurcation. For a sufficiently small $\widetilde{t}_{\mathrm{c}}$, no steady-state solution exists. In the simulation of the spring–slider–dashpot system, the initial condition was selected to be very close to the steady state of larger v^{w}.

To obtain the initial condition, we first numerically solved $F'\left(v^{\mathrm{w}}_{\mathrm{peak}}\right) = 0$ using the grid search and bisection method with the scipy.optimize.bisect. If $F\left(v^{\mathrm{w}}_{\mathrm{peak}}\right) > 0$, a steady-state solution does not exist; thus, we do not conduct a simulation. If $F\left(v^{\mathrm{w}}_{\mathrm{peak}}\right) < 0$, we search for the solution for $F\left(v^{\mathrm{w}}_{\mathrm{ini}}\right) = 0$ using the grid search and bisection method again in the region $v^{\mathrm{w}}_{\mathrm{ini}} > v^{\mathrm{w}}_{\mathrm{peak}}$. From v^{w}_{ini}, we evaluated Θ_{ini} assuming a steady state, and ψ_{ini} from Eqs. (49) and (50), respectively.

3.3 Simulation results

The results of the parameter study are shown in Fig. 6. This result was remarkably similar to that of the continuum model. The boundary between the EQ and ST, as well as the boundary for the existence of a steady-state solution, lies quantitatively close to those plotted in Fig. 2. Figure 7 shows trajectories and the direction of time derivative in the phase space for cases with $\Delta f_* = 0.1875$ and $\widetilde{t}_{\mathrm{c}}$ of ∞, 610, 372.5, 348.75, 87.5, and 63.75 from the panel (a) to (f) together with the steady-state solutions (fixed points). The cases with finite $\widetilde{t}_{\mathrm{c}}$ are indicated by red squares in Fig. 6. In the elastic limit (Fig. 7a), only one fixed point exists: an unstable spiral point indicated by an orange circle. With a relatively large $\widetilde{t}_{\mathrm{c}}$, the other fixed point lies outside the limit cycle of the earthquake cycle (Fig. 7b, c). This fixed point was a saddle point in the simulations conducted in this study. With decreasing $\widetilde{t}_{\mathrm{c}}$, it moved towards the spiral point (Fig. 7c), and the limit cycle disappeared at the EQ–ST boundary (Fig. 7d). With a further decrease in $\widetilde{t}_{\mathrm{c}}$, the saddle point approaches the spiral point (Fig. 7e), and both fixed points disappear together (Fig. 7f) by a tangent bifurcation (Fig. 5) or a saddle-node bifurcation. The cases in Fig. 7e, f are separated by the ST–NoSS boundary. They are different in the number of unstable fixed points and we did not conduct a simulation in the latter case. Nevertheless, the vector field shown in Fig. 7f indicates that the rate-weakening slider gets stuck, and the behavior of the two cases are very similar.

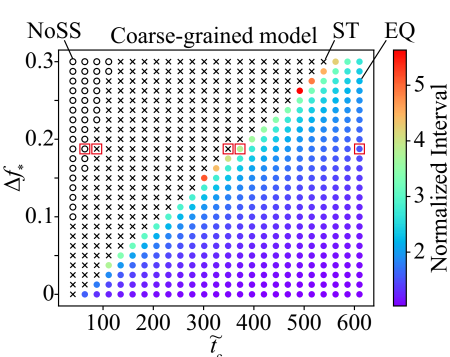

Fig. 6 Result of parameter study for the coarse-grained model. Colors indicate the recurrence interval T_{r} normalized by in the elastic limit. Black crosses and open circles represent permanent stuck and no steady-state solution, respectively. Cases with red squares are plotted in Fig. 7

When the limit cycle disappears, the saddle point touches it and the recurrence interval diverges. This bifurcation is called a homoclinic bifurcation, because the limit cycle starting from a fixed point and returns to the same fixed point is called a homoclinic orbit. The EQ–ST boundary in the coarse-grained model constructed in the present study has been demonstrated as a homoclinic bifurcation, which is qualitatively different from the well-known seismic–aseismic transition explained by a Hopf bifurcation (e.g., Ruina 1983).

4 Discussion

4.1 Comparison of the two models

This study constructed a coarse-grained model from a continuum model based on spatial averages. The parameter studies on t_{c} and Δf_* were performed for both models in comparable manners. As a result, we obtained extremely similar phase diagrams (Figs. 2 and 6) and trajectories for both the EQ (Figs. 3e and 7c) and ST cases (Figs. 3f and 7d). In addition, the boundary between the EQ and SS was quantitatively explained in a previous study (Miyake and Noda 2019) through a similar comparison. Based on these facts, we argue that the behavior of the continuum model can be "understood" using a coarse-grained model. However, we did not directly demonstrate that a homoclinic bifurcation occurred in the continuum model. Miyake and Noda (2019) reported that the recurrence interval of earthquakes diverges when

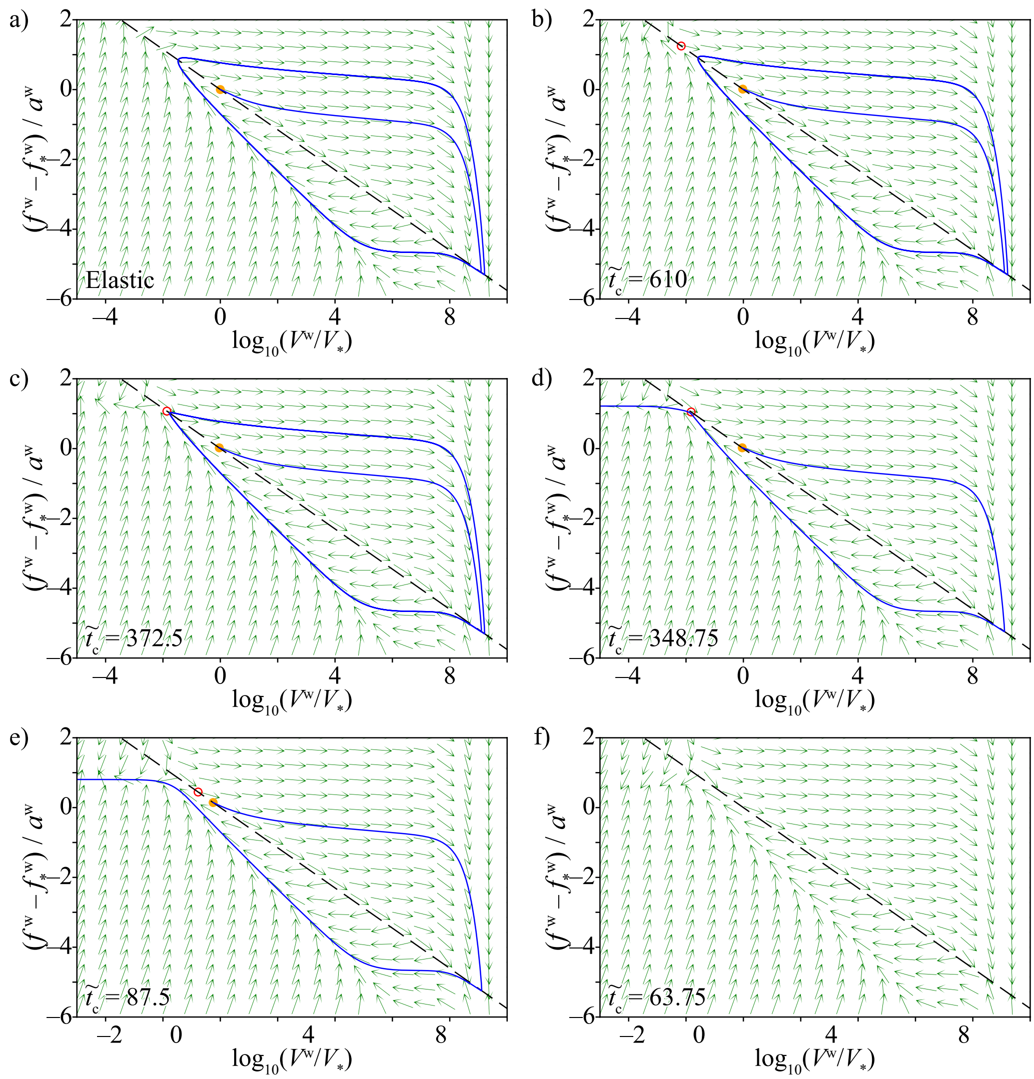

Fig. 7 Trajectories of the elastic limit (**a**) and selected cases (**b–f**) indicated by red squares in Fig. 6 ($\Delta f_* = 0.1875$). Orange and open red circles indicate unstable spiral and saddle points, respectively. Green arrows show the direction of the time derivative

approaching the EQ–ST boundary. This provided supporting evidence for a homoclinic orbit at the transition. Rigorously speaking, to say that the homoclinic bifurcation is responsible for the EQ–ST transition, we have to derive the continuum steady-state solution comparable to the saddle point in the coarse-grained mode, and show that it touches the limit cycle for repeating earthquakes. This is not as straightforward as in the coarse-grained model, which has only two degrees of freedom, and deserves further study.

The coarse grinding performed in this study worked remarkably well. This was probably owing to the relatively small $R/R_c = 2.5$ (Eq. 14). Using ESS with the aging law, Lapusta and Rice (2003) demonstrated that a large R/R_c causes small ruptures that break only a part of the rate-weakening patch. Barbot (2019) also showed that a continuum model with a single rate-weakening patch can undergo period-doubling bifurcation using an ESS with different rate-and-state friction with a single state variable. Earthquakes of multiple sizes cannot occur in the limit cycle of a system with only two degrees of freedom, because the trajectory cannot intersect with itself. Coarse grinding of systems with such complex behavior requires more degrees of freedom. It deserves future study, because it could significantly reduce computational costs in reproducing and even predicting the behavior of a fault hosting repeating earthquake if successful.

4.2 Enhanced relaxation by strength contrast

The strength contrast $\Delta f_* = 0.3$ increases $\widetilde{t}_{\mathrm{c}}$ at the EQ–ST transition by about one order of magnitude (Fig. 2). The effect of the strength contrast can be understood by considering the significance of loading to the rate-weakening patch relative to the amount of the direct effect, similarly to in Miyake and Noda (2019). Let us consider a situation in which the rate-weakening patch is locked, the rate-strengthening region has a slip rate V_{load}, and the stress difference between them is comparable to the strength contrast. Here, we neglect the rate dependency of friction, because it may be a second-order effect compared to the strength contrast. Subsequently, the rate of change in the shear stress in the rate-weakening patch can be written as

$$\dot{\tau} = \frac{\mu V_{\mathrm{load}}}{2R} - \frac{\sigma \Delta f_*}{t_{\mathrm{c}}}, \tag{56}$$

Note that the first and second terms represent elastic loading and VR, respectively, and we omit γ (Eq. 46), which is close to 1. In general, the stress difference between the inside and outside of the rate-weakening patch changes with time. If the slip rates inside and outside the rate-weakening patch is constant, $\dot{\tau}$ decays to zero with a characteristic time of t_{c} and with the net change in the shear stress $t_{\mathrm{c}}\dot{\tau}$. If $t_{\mathrm{c}}\dot{\tau}$ is much smaller than the rate dependency of the fault, the assumption of constant slip rates is approximately applicable and thus we expect no significant acceleration in the locked patch. Therefore, the condition for ST can be written as

$$a^{\mathrm{w}}\sigma \ll t_{\mathrm{c}}\dot{\tau} = \frac{\mu V_{\mathrm{load}} t_{\mathrm{c}}}{2R} - \sigma \Delta f_*. \tag{57}$$

This condition leads to

$$1 \ll \frac{t_{\mathrm{c}}\mu V_{\mathrm{load}}}{2R\sigma\left(a^{\mathrm{w}} + \Delta f_*\right)} = \widetilde{t}_{\mathrm{c}}^{\mathrm{ST}}. \tag{58}$$

Here, $\widetilde{t}_{\mathrm{c}}^{\mathrm{ST}}$ is a newly defined nondimensional relaxation time.

Compared with the non-dimensional relaxation time $\widetilde{t}_{\mathrm{c}}$ defined by Miyake and Noda (2019) (Eq. 26), the new non-dimensional relaxation time $\widetilde{t}_{\mathrm{c}}^{\mathrm{ST}}$ involves the effect of strength contrast. Miyake and Noda (2019) assumed uniform $\Delta f_* = 0$ and used V_* for V_{load} as an approximation partly because a steady-state solution with uniform $V = V_*$ exists. However, in the present study, V in the steady-state solution was not necessarily uniform, and a simple approximation of V_{load} was difficult to obtain.

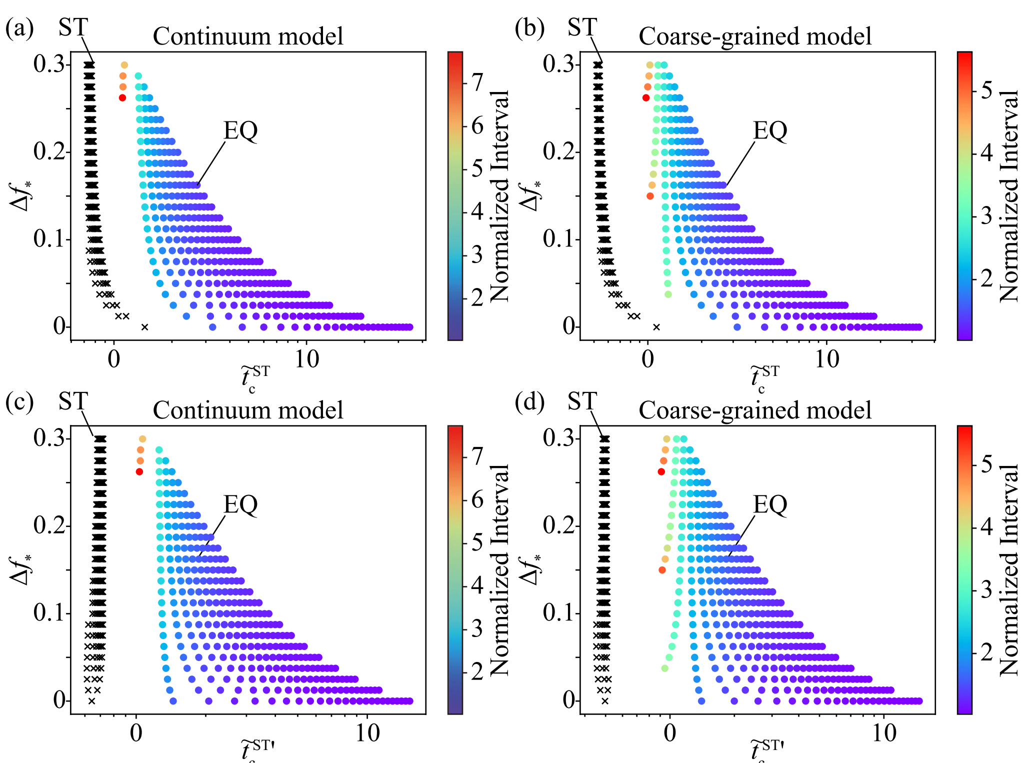

Fig. 8 System behavior to Fig. 2 (left column) and Fig. 6 (right column) but plotted as functions of newly defined nondimensional relaxation time $\widetilde{t}_{\mathrm{c}}^{\mathrm{ST}}$ (upper row) and $\widetilde{t}_{\mathrm{c}}^{\mathrm{ST}\prime}$ (lower row)

Therefore, we adopted for V_{load} the minimum value of V at the center of the rate-strengthening region (minimum x) for the continuum model. The minimum value of V^{s} was adopted for the coarse-grained model. Although these values cannot be obtained a priori, this study aims to evaluate the conditions in Eq. (58) to validate the theory behind it and understand the effect of strength contrast.

Figure 8a, b shows the behavior of the continuum and coarse-grained models, similar to Figs. 2 and 6, respectively, as a function of the new non-dimensional relaxation time $\widetilde{t}_{\mathrm{c}}^{\mathrm{ST}}$. The boundary between ST and EQ lies at approximately $\widetilde{t}_{\mathrm{c}}^{\mathrm{ST}} = 1$, indicating that Eq. (58) condition works remarkably well at the EQ–ST boundary. For extremely small strength contrast (say, $\Delta f_* < 0.05$), the boundary shifts in the direction of large $\widetilde{t}_{\mathrm{c}}^{\mathrm{ST}}$ and moves to around $\widetilde{t}_{\mathrm{c}}^{\mathrm{ST}} = 2$ at $\Delta f_* = 0$. In formulating Eq. (56), we estimated the effect of VR only from the contribution of Δf_* and neglected that from frictional rate dependency. Even with $\Delta f_* = 0$, regions with different slip rates such as creeping and locked regions have different shear stress. The boundary can be straightened by adding a small number to Δf_* to account for this effect in the definition of $\widetilde{t}_{\mathrm{c}}^{\mathrm{ST}}$ (Eq. 58). In Fig. 8c, d, the horizontal axes represent:

$$\widetilde{t}_{\mathrm{c}}^{\mathrm{ST}'} = \frac{t_{\mathrm{c}} \mu V_{\mathrm{load}}}{2R\sigma \left(a^{\mathrm{w}} + \Delta f_* + 0.02\right)}. \tag{59}$$

At this point, we were confident that the EQ–ST boundary could be explained by the significance of the loading rate to the rate-weakening patch, which is the sum of the contributions from elastic loading due to creep in the rate-strengthening region and from VR. Note that this explanation simply interprets the simulation results and does not mathematically indicate the condition for the homoclinic bifurcation discussed in the previous section.

4.3 Implication to observations

The model shows that a stronger patch favors ST and has a lower long-term slip rate, whereas a weaker region exhibits a higher long-term slip rate (Fig. 3a, b). The anti-correlation between the strength and slip rate is a consequence of VR, which causes unloading and loading in the stronger and weaker parts of the fault, respectively. The heterogeneous long-term slip rate is difficult to observe geodetically. Although the slip rate of the stronger patch was low, viscous deformation was concentrated around it, forming a distributed shear zone. The coexistence of localized frictional slip and distributed shear deformation is, by definition, a characteristic of the brittle–ductile transitional regime. Modeling frictional surfaces embedded in a viscously deformable medium is important for understanding geophysically observable phenomena and rock textures in the brittle–ductile transition.

Our simulations suggest that a patch with large $\widetilde{t}_{\mathrm{c}}^{\mathrm{ST}} \gg 1$ generates repeating earthquakes, while that with small $\widetilde{t}_{\mathrm{c}}^{\mathrm{ST}} \ll 1$ is stuck and seismically silent. Because $\widetilde{t}_{\mathrm{c}}^{\mathrm{ST}}$ is inversely proportional to R, it is expected that a larger rate-weakening patch will become aseismic earlier than a smaller patch as the viscosity of the medium decreases, as pointed out by Miyake and Noda (2019). Spada et al. (2013) reported the depth variation of the Gutenberg–Richter (GR) b value for several regions of the world and showed that it increases with depth, at least in some places below 15 km, which is around the brittle–plastic transition (e.g., Sibson 1983; Scholz 1988). A larger GR b value indicated a smaller fraction of large earthquakes in the set of earthquakes. Yamaguchi et al. (2011) conducted friction experiments using a silicone gel plate that hosted force drop events of various amplitudes in a laboratory experiment. They calculated the power-law decay rate of the frequency-size distribution of these events and reported that efficient viscoelasticity reduces the fraction of large events. The results of the present study agree qualitatively with these reports. However, we analyzed a system with only one rate-weakening patch, and seismicity is often clustered (e.g., mainshock–aftershock sequences and earthquake swarms). Thus, the interaction of seismogenic patches may be important. Further quantitative analyses are required to determine whether VR plays an important role in natural seismic–aseismic transitions.

5 Conclusion

A previous study (Miyake and Noda 2019) discovered a transition between repeating earthquakes (EQ) and permanent stuck (ST) for a rate-and-state fault embedded in a viscoelastic medium (EQ–ST transition). This differs from the well-known transition explained by comparing the critical stiffness and stiffness of the elastic system, which is accompanied by Hopf bifurcation (Ruina 1983). In a viscoelastic medium, the heterogeneous fault frictional strength matters, unlike in an elastic medium, because the resulting stress heterogeneity relaxes with time, causing loading and unloading to weaker and stronger regions, respectively. In the present study, we performed dynamic earthquake sequence simulations for a rate-and-state fault in a viscoelastic medium with strength contrast inside and outside a rate-weakening patch to better understand the EQ–ST transition, to investigate the effect of strength contrast, and to draw a physical understanding of system behavior.

Experimental studies have suggested that a rate-weakening patch has a potentially larger frictional resistance than a rate-strengthening patch (e.g., Ikari et al. 2011). A parameter study in terms of the frictional strength contrast Δf_* and the viscoelastic relaxation time t_c showed that $\Delta f_* = 0.3$ causes the EQ–ST transition at about 1 order of magnitude larger t_c than in the case with $\Delta f_* = 0$. Because the continuum model has many degrees of freedom, which makes a mathematically rigorous discussion difficult, we developed a coarse-grained model based on spatial averaging and compared the two models. The coarse-grained model showed a quantitatively similar behavior; thus, we investigated the EQ–ST transition in this model in detail. We found that the EQ–ST transition is realized by homoclinic bifurcation, in which a saddle point touches a stable limit cycle. To our knowledge, this is the first time to point out the possibility of a seismic–aseismic transition by homoclinic bifurcation.

We also quantitatively explained the EQ–ST boundary by comparing loading rate $\dot{\tau}$ to the rate-weakening patch and the frictional instantaneous rate dependency. In addition to the elastic loading due to creep in the rate-strengthening region, the viscoelastic relaxation of stress heterogeneity contributes to $\dot{\tau}$. We defined a nondimensional relaxation time $\widetilde{t}_c^{ST}$, which is proportional to t_c, inversely proportional to the patch radius R, and correlate negatively with Δf_*, to show that the EQ–ST boundary lies around $\widetilde{t}_c^{ST} = 1$. As the viscoelastic relaxation became significant, a large rate-weakening patch became aseismic before a small patch. This behavior is qualitatively consistent with an increase in the Gutenberg–Richter b value near the deeper end of the seismogenic layer (e.g., Spada et al. 2013), but further investigations on, for example, the effects of earthquake interactions and changes in frictional parameters with depth are required for quantitative discussion.

Abbreviations

EQ	Repeating earthquakes
AT	Aseismic transients
SS	Steady-state slip
ST	Permanent stuck
SBIEM	Spectral boundary integral equation method

Acknowledgements
The authors would like to thank the editors and reviewers for useful comments in improving the manuscript.

Author contributions
Hiroyuki Noda developed the method, conceptualized the study, coded the simulation program for the continuum model, designed the parameter study, contributed to the theoretical analysis, and created the original draft. Makoto Yamamoto coded the simulation program for the coarse-grained model, adapted the simulation programs for the parameter study, conducted the parameter study, analyzed the numerical results, and contributed to the theoretical analysis.

Funding
This study was supported by the Ministry of Education, Culture, Sports, Science and Technology (MEXT) of Japan under its Third Earthquake and Volcano Hazards Observation and Research Program (Earthquake and Volcano Hazard Reduction Research) and by JSPS KAKENHI Grant Number 21H05201.

Availability of data and materials
Observational data were not used in the present study. The simulation code used in the study is available upon reasonable request.

Declarations

Ethics approval and consent to participate
Not applicable.

Consent for publication
Not applicable.

Competing interests
The author does not have any competing interests.

Author details
[1]Disaster Prevention Research Institute, Kyoto University, Gokasho, Uji 6110011, Japan. [2]Daikin Industries, Ltd., Osaka 530-0001, Japan.

Received: 31 July 2024 Accepted: 8 November 2024
Published online: 29 November 2024

References

Allison KL, Dunham EM (2018) Earthquake cycle simulations with rate-and-state friction and power-law viscoelasticity. Tectonophysics 733:232–256. https://doi.org/10.1016/j.tecto.2017.10.021

Ando R, Yamashita T (2007) Effects of mesoscopic-scale fault structure on dynamic earthquake ruptures: dynamic formation of geometrical complexity of earthquake faults. J Geophys Res Solid Earth 112:B09303. https://doi.org/10.1029/2006JB004612

Andrews DJ (2005) Rupture dynamics with energy loss outside the slip zone. J Geophys Res Solid Earth 110:B01307. https://doi.org/10.1029/2004JB003191

Barbot S (2019) Slow-slip, slow earthquakes, period-two cycles, full and partial ruptures, and deterministic chaos in a single asperity fault. Tectonophysics 768:228171. https://doi.org/10.1016/j.tecto.2019.228171

Beeler NM, Tullis TE, Blanpied ML, Weeks JD (1996) Frictional behavior of large displacement experimental faults. J Geophys Res Solid Earth 101:8697–8715. https://doi.org/10.1029/96JB00411

Blanpied ML, Marone CJ, Lockner DA et al (1998) Quantitative measure of the variation in fault rheology due to fluid–rock interactions. J Geophys Res Solid Earth 103:9691–9712. https://doi.org/10.1029/98JB00162

Byerlee J (1978) Friction of rocks. Pure Appl Geophys 116:615–626. https://doi.org/10.1007/BF00876528

Collettini C, Niemeijer A, Viti C, Marone C (2009) Fault zone fabric and fault weakness. Nature 462:907–910. https://doi.org/10.1038/nature08585

Day SM, Dalguer LA, Lapusta N, Liu Y (2005) Comparison of finite difference and boundary integral solutions to three-dimensional spontaneous rupture. J Geophys Res Solid Earth 110:B12307. https://doi.org/10.1029/2005JB003813

den Hartog SAM, Niemeijer AR, Spiers CJ (2012) New constraints on megathrust slip stability under subduction zone P-T conditions. Earth Planet Sci Lett 353–354:240–252. https://doi.org/10.1016/j.epsl.2012.08.022

Dieterich JH (1979) Modeling of rock friction: 1. Experimental results and constitutive equations. J Geophys Res Solid Earth 84:2161–2168. https://doi.org/10.1029/JB084iB05p02161

Dublanchet P, Bernard P, Favreau P (2013) Interactions and triggering in a 3-D rate-and-state asperity model. J Geophys Res Solid Earth 118:2225–2245. https://doi.org/10.1002/jgrb.50187

Goswami A, Barbot S (2018) Slow-slip events in semi-brittle serpentinite fault zones. Sci Rep 8:6181. https://doi.org/10.1038/s41598-018-24637-z

Gu J-C, Rice JR, Ruina AL, Tse ST (1984) Slip motion and stability of a single degree of freedom elastic system with rate and state dependent friction. J Mech Phys Solids 32:167–196. https://doi.org/10.1016/0022-5096(84)90007-3

Iio Y, Sagiya T, Kobayashi Y, Shiozaki I (2002) Water-weakened lower crust and its role in the concentrated deformation in the Japanese Islands. Earth

Planet Sci Lett 203:245–253. https://doi.org/10.1016/S0012-821X(02)00879-8
Ikari MJ, Saffer DM, Marone C (2009) Frictional and hydrologic properties of clay-rich fault gouge. J Geophys Res Solid Earth 114:B05409. https://doi.org/10.1029/2008JB006089
Ikari MJ, Marone C, Saffer DM (2011) On the relation between fault strength and frictional stability. Geology 39:83–86. https://doi.org/10.1130/G31416.1
Johnson KM, Tebo D (2018) Capturing 50 years of postseismic mantle flow at Nankai subduction zone. J Geophys Res Solid Earth 123:10091–10106. https://doi.org/10.1029/2018JB016345
Kato N (2003) Repeating slip events at a circular asperity: numerical simulation with a rate- and state-dependent friction law. Bull Earthq Res Inst Univ Tokyo 78:151–166
Lapusta N, Liu Y (2009) Three-dimensional boundary integral modeling of spontaneous earthquake sequences and aseismic slip. J Geophys Res Solid Earth 114:B09303. https://doi.org/10.1029/2008JB005934
Lapusta N, Rice JR (2003) Nucleation and early seismic propagation of small and large events in a crustal earthquake model. J Geophys Res Solid Earth 108:2205. https://doi.org/10.1029/2001JB000793
Lapusta N, Rice JR, Ben-Zion Y, Zheng G (2000) Elastodynamic analysis for slow tectonic loading with spontaneous rupture episodes on faults with rate- and state-dependent friction. J Geophys Res Solid Earth 105:23765–23789. https://doi.org/10.1029/2000JB900250
Liu Y, Rice JR (2007) Spontaneous and triggered aseismic deformation transients in a subduction fault model. J Geophys Res Solid Earth 112:B09404. https://doi.org/10.1029/2007JB004930
Miyake Y, Noda H (2019) Fully dynamic earthquake sequence simulation of a fault in a viscoelastic medium using a spectral boundary integral equation method: does interseismic stress relaxation promote aseismic transients? Earth Planet Space 71:137. https://doi.org/10.1186/s40623-019-1113-8
Moore JDP, Yu H, Tang C-H et al (2017) Imaging the distribution of transient viscosity after the 2016 Mw 7.1 Kumamoto earthquake. Science 356:163–167. https://doi.org/10.1126/science.aal3422
Noda H, Lapusta N (2010) Three-dimensional earthquake sequence simulations with evolving temperature and pore pressure due to shear heating: effect of heterogeneous hydraulic diffusivity. J Geophys Res Solid Earth 115:B12314. https://doi.org/10.1029/2010JB007780
Noda H, Sawai M, Shibazaki B (2017) Earthquake sequence simulations with measured properties for JFAST core samples. Philos Trans A Math Phys Eng Sci 375:20160003. https://doi.org/10.1098/rsta.2016.0003
Obara K, Kato A (2016) Connecting slow earthquakes to huge earthquakes. Science 353:253–257. https://doi.org/10.1126/science.aaf1512
Okubo K, Bhat HS, Rougier E et al (2019) Dynamics, radiation, and overall energy budget of earthquake rupture with coseismic off-fault damage. J Geophys Res Solid Earth 124:11771–11801. https://doi.org/10.1029/2019JB017304
Rice JR (1993) Spatio-temporal complexity of slip on a fault. J Geophys Res Solid Earth 98:9885–9907. https://doi.org/10.1029/93JB00191
Rice JR, Ben-Zion Y (1996) Slip complexity in earthquake fault models. Proc Natl Acad Sci U S A 93:3811–3818. https://doi.org/10.1073/pnas.93.9.3811
Rubin AM, Ampuero J-P (2005) Earthquake nucleation on (aging) rate and state faults. J Geophys Res Solid Earth 110:B11312. https://doi.org/10.1029/2005JB003686
Ruina A (1983) Slip instability and state variable friction laws. J Geophys Res Solid Earth 88:10359–10370. https://doi.org/10.1029/JB088iB12p10359
Saffer DM, Marone C (2003) Comparison of smectite- and illite-rich gouge frictional properties: application to the updip limit of the seismogenic zone along subduction megathrusts. Earth Planet Sci Lett 215:219–235. https://doi.org/10.1016/S0012-821X(03)00424-2
Savage JC, Prescott WH (1978) Asthenosphere readjustment and the earthquake cycle. J Geophys Res Solid Earth 83:3369–3376. https://doi.org/10.1029/JB083iB07p03369
Sawai M, Niemeijer AR, Plümper O et al (2016) Nucleation of frictional instability caused by fluid pressurization in subducted blueschist. Geophys Res Lett 43:2543–2551. https://doi.org/10.1002/2015GL067569
Scholz CH (1988) The brittle-plastic transition and the depth of seismic faulting. Geol Rundsch 77:319–328. https://doi.org/10.1007/BF01848693
Segall P, Rice JR (1995) Dilatancy, compaction, and slip instability of a fluid-infiltrated fault. J Geophys Res Solid Earth 100:22155–22171. https://doi.org/10.1029/95JB02403
Segall P, Rubin AM, Bradley AM, Rice JR (2010) Dilatant strengthening as a mechanism for slow slip events. J Geophys Res Solid Earth 115:B12305. https://doi.org/10.1029/2010JB007449
Shelly DR (2009) Possible deep fault slip preceding the 2004 Parkfield earthquake, inferred from detailed observations of tectonic tremor. Geophys Res Lett 36:L17318. https://doi.org/10.1029/2009GL039589
Shibazaki B, Shimamoto T (2007) Modelling of short-interval silent slip events in deeper subduction interfaces considering the frictional properties at the unstable—stable transition regime. Geophys J Int 171:191–205. https://doi.org/10.1111/j.1365-246X.2007.03434.x
Sibson RH (1983) Continental fault structure and the shallow earthquake source. J Geol Soc Lond 140:741–767. https://doi.org/10.1144/gsjgs.140.5.0741
Spada M, Tormann T, Wiemer S, Enescu B (2013) Generic dependence of the frequency-size distribution of earthquakes on depth and its relation to the strength profile of the crust. Geophys Res Lett 40:709–714. https://doi.org/10.1029/2012GL054198
Templeton EL, Rice JR (2008) Off-fault plasticity and earthquake rupture dynamics: 1. Dry materials or neglect of fluid pressure changes. J Geophys Res Solid Earth 113:B09306. https://doi.org/10.1029/2007JB005529
Thatcher W, Rundle JB (1984) A viscoelastic coupling model for the cyclic deformation due to periodically repeated Earthquakes at subduction zones. J Geophys Res Solid Earth 89:7631–7640. https://doi.org/10.1029/JB089iB09p07631
Wang K, Hu Y, He J (2012) Deformation cycles of subduction earthquakes in a viscoelastic Earth. Nature 484:327–332. https://doi.org/10.1038/nature11032
Yamaguchi T, Morishita M, Doi M et al (2011) Gutenberg–Richter's law in sliding friction of gels. J Geophys Res Solid Earth 116:B12306. https://doi.org/10.1029/2011JB008415

Publisher's Note